Supporting Information

Inducing Hollow and Porous Hematite Nanorod Photoanodes by Rare Earth and Transition Metal Doping for Enhanced Solar Water Splitting

Chenyang Xu,‡[a] Hongxin Wang,‡[a] Ke Liang,[a] Yuanming Zhang[a], Weicong Li[a] and Hemin Zhang[ab]*

[a]College of Materials Science and Engineering, Sichuan University, Chengdu 610065, China

[b]Engineering Research Center of Alternative Energy Materials and Devices, Ministry of Education, Sichuan University, Chengdu 610065, China

*Email: hmzhang@scu.edu.cn

Experimental

Synthesis of Nb:FeOOH@Eu:FeOOH Core−shell Nanorods on FTO Substrate

The synthesis of β-FeOOH nanorod films on FTO (TEC8, 6−9 Ω, Pilkington) was carried out through a straightforward hydrothermal method. A piece of FTO glass underwent ultrasonic cleaning in deionized water, ethanol, and acetone to ensure a sufficiently hydrophilic surface. The core part of Nb:FeOOH nanorods grew on the FTO substrate in a 25 mL aqueous solution containing 0.15 M $FeCl_3 \cdot 6H_2O$ (Aladdin, 99.0%), 1 M $NaNO_3$ (Aladdin, 99.0%), 200 μL HNO_3 (Aladdin, 50%), and varied amounts of $NbCl_5$ (Aladdin, 99.99%) solution at 100 °C for 3 h. The obtained yellow Nb:FeOOH nanorod film was rinsed thoroughly with deionized water. Subsequently, a solution-based re-growth of the Eu:FeOOH conformal shell on the surface of Nb:FeOOH nanorods was conducted in the same solution with different amounts of $EuCl_3 \cdot 6H_2O$ (Aladdin, 99.99%) solution replacing $NbCl_5$ at 100 °C for 1 h. Finally, the prepared core−shell Nb:FeOOH@Eu:FeOOH nanorods on FTO were thoroughly rinsed with deionized water.

Fabrication of Hollow-structured Eu, Nb Co-doped Hematite Nanorods by Hybrid Microwave Annealing (HMA)

The Nb:FeOOH@Eu:FeOOH core−shell nanorods on FTO were placed on 70 mL graphite powder as a susceptor in a Pyrex beaker (100 mL) and subjected to treat in a household microwave oven (2.45 GHz, 1000 W) for 2−3 min at full power. By HMA treatment, the Nb:FeOOH@Eu:FeOOH nanorods were transformed into hollow-structured Eu, Nb co-doped hematite (Eu,Nb:Fe_2O_3) nanorods without significant alteration in morphology.

Loading of A $RuFe_2(OH)_x$ Co-catalyst

The fabricated Eu,Nb:Fe_2O_3 photoelectrode was submerged in an aqueous solution containing 5 mM $RuCl_3 \cdot 3H_2O$ (Aladdin, 98%) and 10 mM $FeCl_3 \cdot 6H_2O$ (Aladdin, 99%) for 10 min at room

temperature. Subsequently, the electrode was rinsed by 1 M NaOH solution immediately for several seconds to form their hydroxide.

Physical Characterization

The morphology and corresponding energy-dispersive X-ray spectroscopy (EDS) were performed by scanning electron microscope (SEM, Sigma 300, Zeiss, Germany). High-resolution transmission electron microscopy (HRTEM) images, high-angle annular dark-field TEM (HAADF-TEM) images and corresponding EDS mappings were taken by a FEI Talos F200X G2 microscope. X-ray diffraction (XRD) spectra were obtained by Empyrean XRD, using Cu-K_α (λ = 1.5406 Å) radiation at 40 kV and 40 mA. The electron paramagnetic resonance (EPR) was achieved by Bruker EMXplus 9.5/12. The surface element composition and depth profiling were achieved by X-ray photoelectron spectroscopy (XPS, KRATOS, Axis Ultra^{DLD}, Al K_α). Ultraviolet-visible absorbance (UV−vis) was conducted on a UV−vis spectrometer (Shimadzu UV-3600i Plus). Steady state photoluminescence (PL) measurements were performed on a spectrofluorometer (HORIBA FluoroMax-4) with an excitation wavelength of 450 nm using a 150 W Xenon lamp as the excitation source.

Photoelectrochemical Measurements

All (photo)electrochemical measurements were conducted on a potentiostat (IviumStat.h, Ivium Technologies) under the simulated AM 1.5 G (100 mW cm^{-2}) illumination, in 1 M NaOH electrolyte in a three-electrode cell with the photoanode, Ag/AgCl, and Pt mesh as working, reference, and counter electrodes, respectively. The potentials for *J*−*V* curves were swept from 0.4 to 1.8 V_{RHE} at a scanning rate of 20 mV s^{-1}. All the measured potentials vs. Ag/AgCl reference electrode were converted to the potentials vs. reversible hydrogen electrode (RHE) by the Nernst equation

$$E_{RHE} = E_{Ag/AgCl} + 0.0592\ pH + E^{o}_{Ag/AgCl}\ (E^{o}_{Ag/AgCl} = 0.1976 \text{ at } 25\ ^{\circ}C) \quad (1)$$

The photoelectrochemical impedance spectroscopy (PEIS) spectra were acquired at 1.23 V_{RHE}

under simulated 1-sun condition with a frequency range of 100 kHz−0.1 Hz. A Z-View software (Scribner Associates) was used for fitting the experimental PEIS data to an equivalent circuit model. The Mott−Schottky plots were obtained by potential sweeping from 0.1 to 1.0 V_{RHE} with AC frequency of 1000 Hz without illumination.

The open circuit potential (OCP) transient decay was measured in the same experimental condition as PEC measurements. The carrier lifetime can be quantified by the equation[1]

$$\tau_n = -\frac{k_B T}{e}\left(\frac{dOCP}{dt}\right)^{-1} \quad (2)$$

where τ_n, k_B, T, e, and dOCP/dt are the carrier lifetime, Boltzmann's constant, temperature (K), charge of single electron, and derivative of the OCP transient decay, respectively.

The incident photon-to-current conversion efficiency (IPCE) measurement is carried on a 300 W Xe lamp (equipped with AM 1.5 G filter) and a monochromator (Newport, CS260B) with a band width of 10 nm. IPCE can be calculated from the measured current density according to the equation

$$\mathrm{IPCE} = \frac{1240 \times J\,(\mathrm{mA\ cm^{-2}})}{P_{light}\,(\mathrm{mW\ cm^{-2}}) \times \lambda\,(\mathrm{nm})} \quad (3)$$

where J is the measured current density at specific wavelength, λ is the specific wavelength of incident light, and P_{light} is the corresponding calibrated illumination power.

The donor density N_D is inversely proportional to the slope of the M−S plot and can be extracted from the equation[2]

$$\left(\frac{A}{C}\right)^2 = \frac{2}{q\varepsilon_r\varepsilon_0 N_D}\left(V - E_{FB} - \frac{k_B T}{q}\right) \quad (4)$$

where A is the surface area of photoanode, C is the capacitance of photoanode (C_{bulk} + C_{ss}). V is the applied potential, E_{FB} is the flat band potential, $k_B = 1.38 \times 10^{-23}$ J K^{-1}, T = 298 K, q = 1.602×10^{-19} C, $\varepsilon_0 = 8.85 \times 10^{-12}$ C^2 J^{-1} m^{-1}, and $\varepsilon_r = 32$ for hematite.

The depletion width (W_d) stands as a critical parameter in evaluating PEC performance of photoelectrodes, and can be calculated with the equation[3]

$$W_d = \left(\frac{2\varepsilon_r\varepsilon_0 V_{bi}}{qN_D}\right)^{1/2} \quad (5)$$

where V_{bi} is the built-in potential, which can be calculated by subtracting E_{FB} from E_A (applied potential).

Supporting Figures

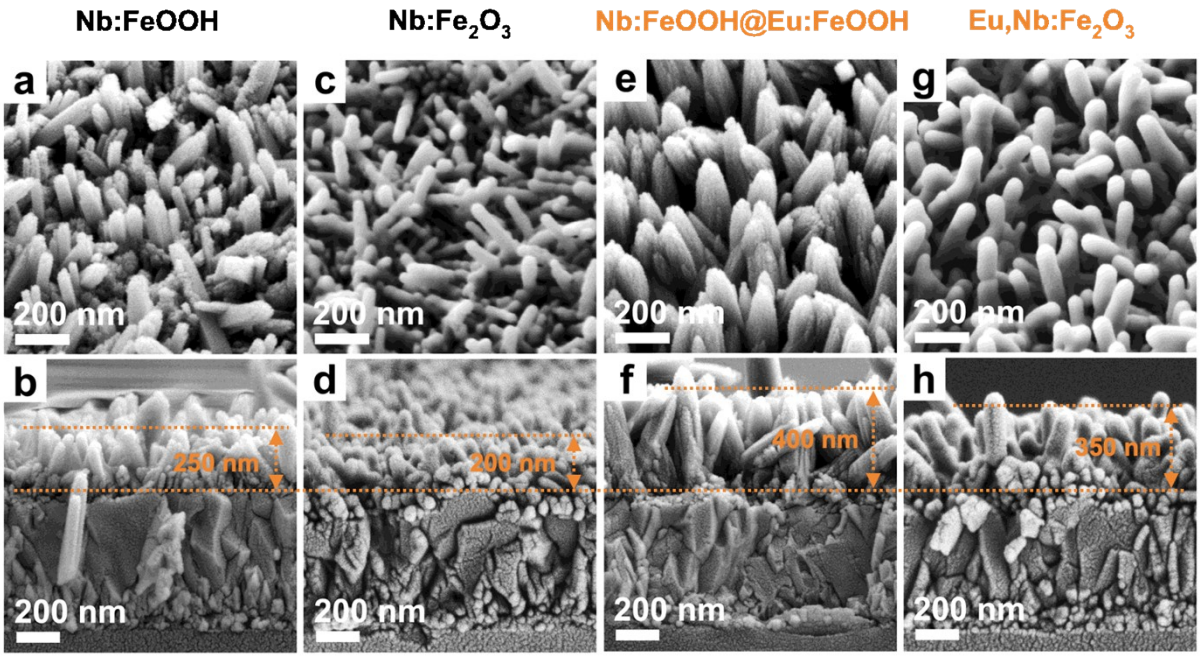

Figure S1. SEM morphologies of (a, b) Nb:FeOOH, (c, d) Nb:Fe_2O_3, (e, f) Nb:FeOOH@Eu:FeOOH and (g, h) Eu,Nb:Fe_2O_3 nanorods. After HMA, the surface structure was reconfigured by extremely high-temperature and rapidly heating, resulting in a smoother surface for all samples and a noticeable reduction in nanorod diameters due to dehydration and conversion into hematite.

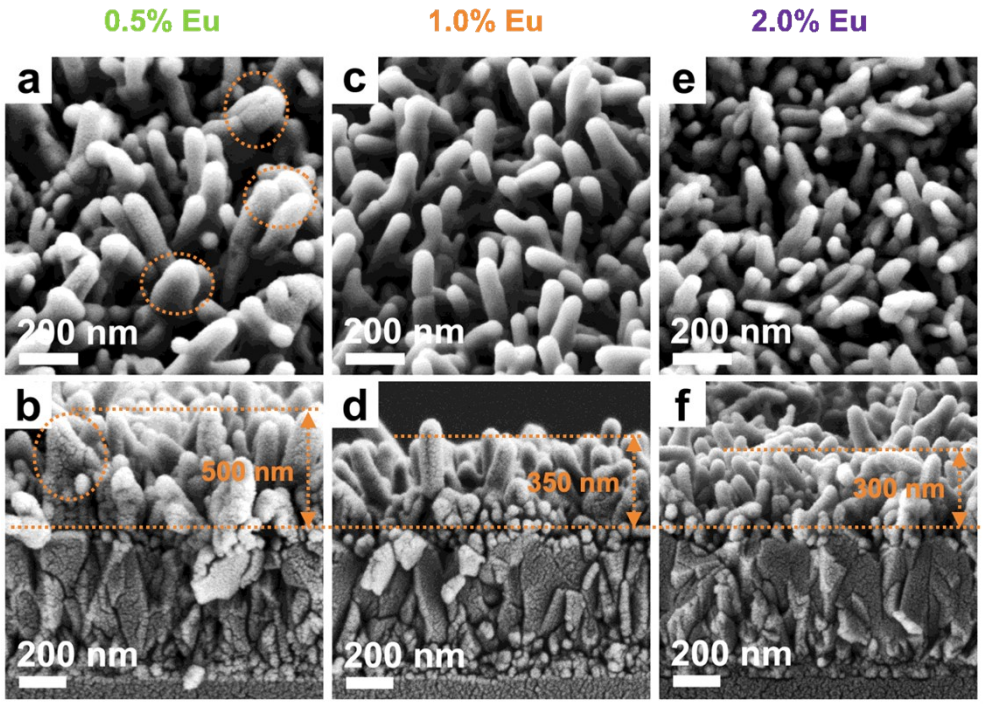

Figure S2. SEM morphologies of Eu,Nb:Fe_2O_3 nanorods by HMA with different Eu concentration. The re-growth of an Eu:FeOOH shell on Nb:FeOOH nanorods with Eu concentrations (Eu/Fe) of (a, b) 0.5%, (c, d) 1.0% and (e, f) 2.0%. The increase of Eu^{3+} ion concentration intensifies solute drag effect and inhibits the OA process, resulting in smaller diameters of nanorods. Higher Eu^{3+} ion concentrations (1.0%, 2.0%) exhibit effective nanostructure preservation during HMA, while a lower one leads to the fusion tips of nanorods.

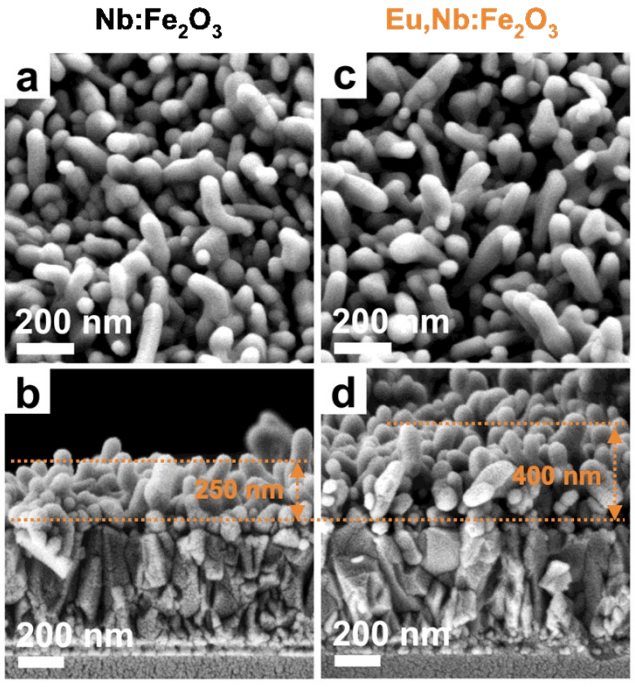

Figure S3. SEM morphologies of (a, b) Nb:Fe_2O_3 and (c, d) Eu,Nb:Fe_2O_3 nanorods by CTA.

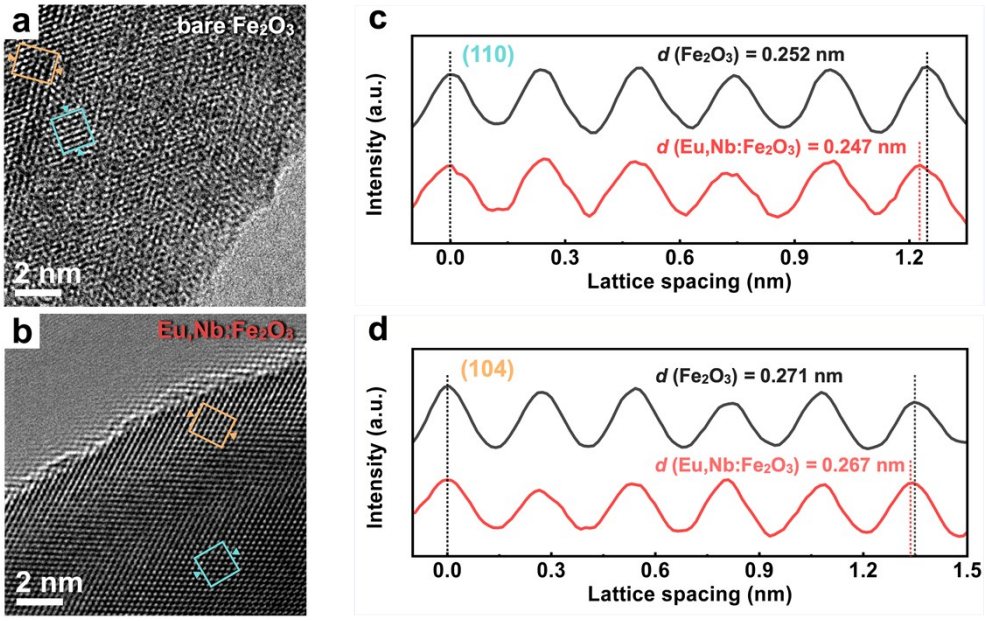

Figure S4. HRTEM images of (a) bare Fe_2O_3 and (b) Eu,Nb:Fe_2O_3 nanorods. Derived *d*-spacing patterns of (c) (110) crystal planes marked as blue squares and (d) (104) crystal planes marked as yellow squares in HRTEM images.

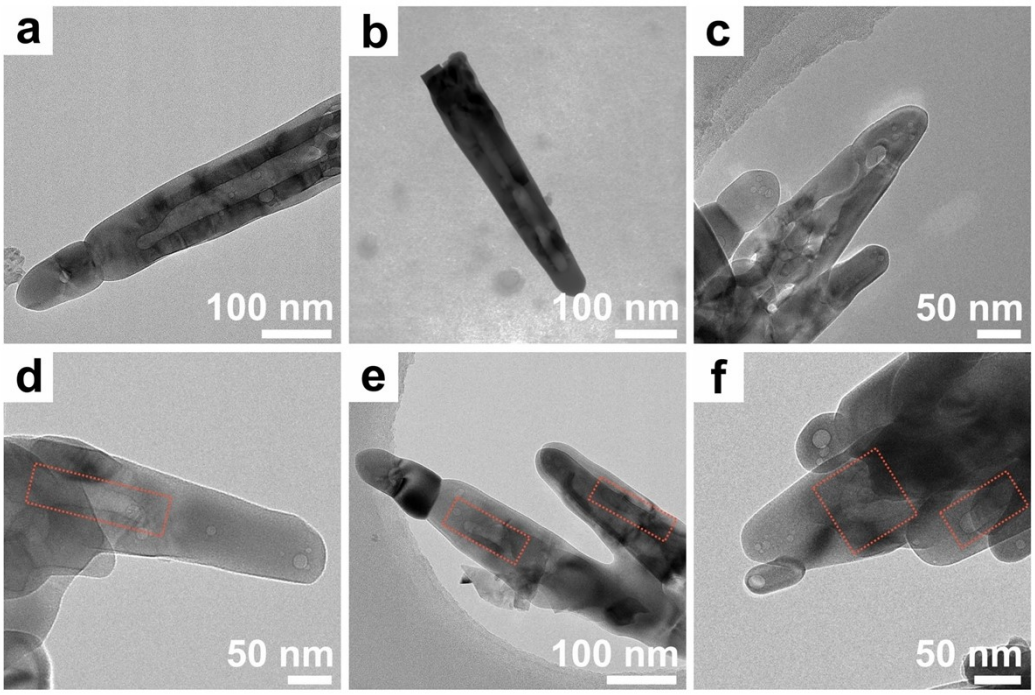

Figure S5. TEM images of hollow Eu,Nb:Fe_2O_3 nanorods by HMA. The HRTEM images and EDS analysis in Fig. 2c–i are obtained from (a), and more evidences of hollow structure in Eu,Nb:Fe_2O_3 nanorods are provided in (b–f).

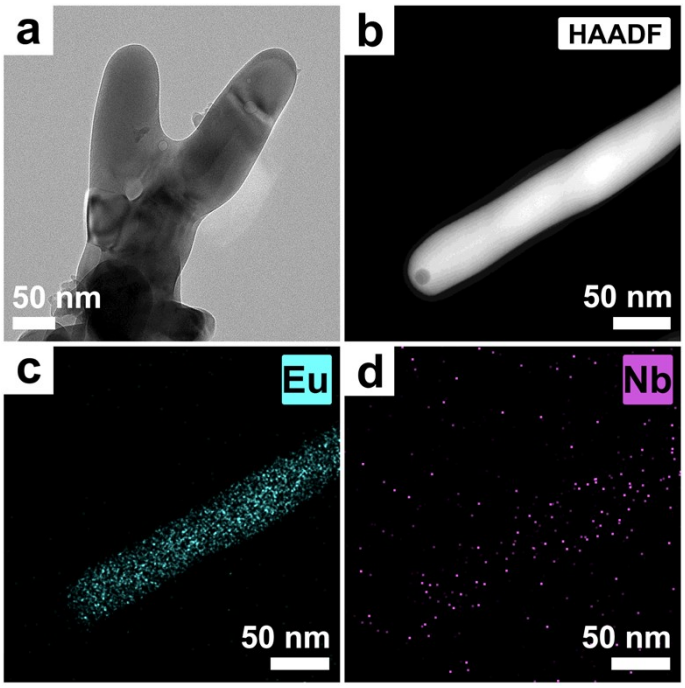

Figure S6. (a) TEM image, (b) HAADF and (c, d) EDS mappings of solid Eu,Nb:Fe_2O_3 nanorods after CTA.

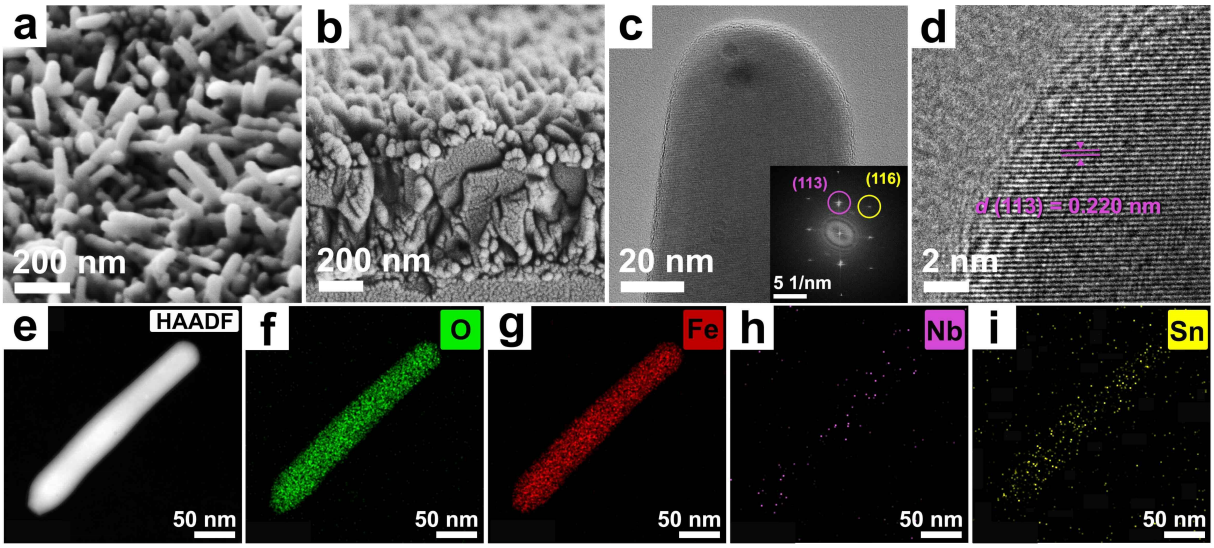

Figure S7. (a) Top and (b) cross-section views of SEM, (c, d) HRTEM, (e) HAADF and (f–i) EDS mappings of Nb:Fe_2O_3 nanorod by HMA.

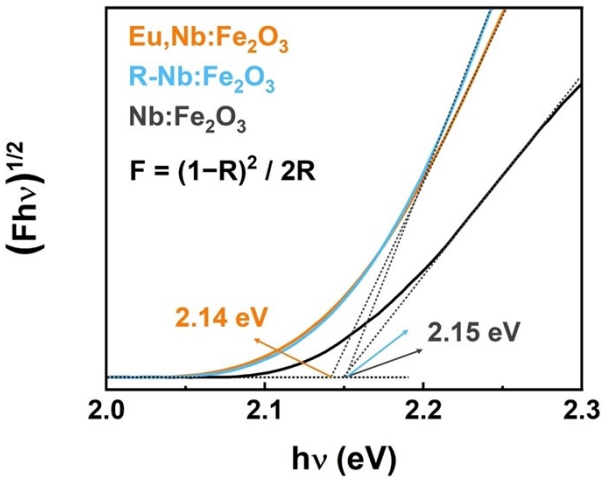

Figure S8. Tauc plots of $Nb:Fe_2O_3$, $R\text{-}Nb:Fe_2O_3$ and $Eu,Nb:Fe_2O_3$ by HMA.

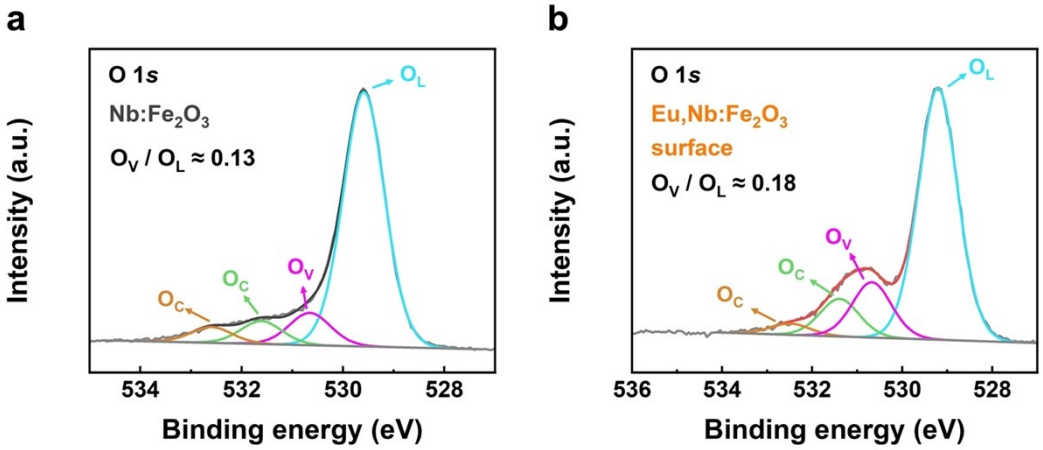

Figure S9. Surface O 1*s* XPS of (a) $Nb:Fe_2O_3$ and (b) $Eu,Nb:Fe_2O_3$. The O 1*s* peaks can be fitted with three or four distinct peaks corresponding to lattice oxygen (O_L, 529.5−530.0 eV), oxygen vacancies (O_V, 531.0−531.6 eV), and chemisorbed oxygen (O_C, 532.5−533.1 eV).[4]

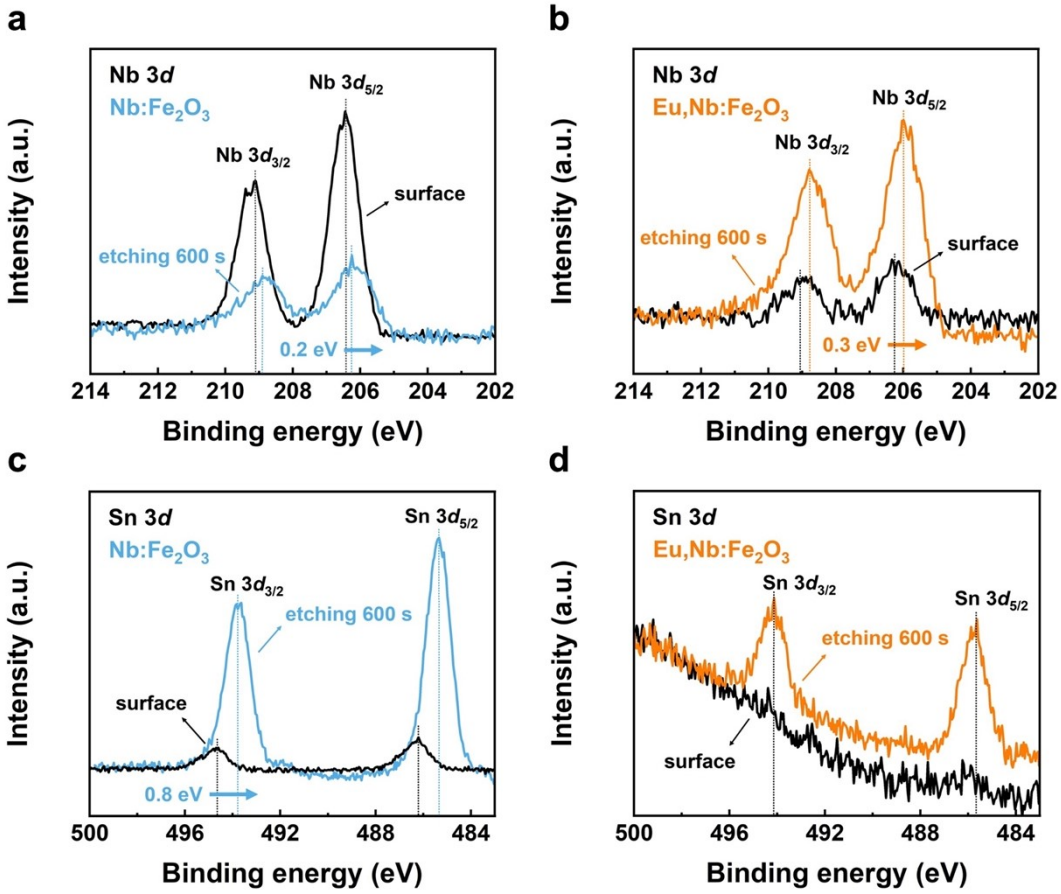

Figure S10. Nb 3*d* XPS depth profiles (etching 0 s and 600 s by Ar^+) of (a) Nb:Fe_2O_3 and (b) Eu,Nb:Fe_2O_3. Sn 3*d* XPS depth profiles (etching 0 s and 600 s by Ar^+) of (c) Nb:Fe_2O_3 and (d) Eu,Nb:Fe_2O_3. In the Nb 3*d* XPS spectra, all samples show Nb $3d_{3/2}$ (208.8−209.1 eV) and Nb $3d_{5/2}$ (206.1−206.4 eV) peaks as typical for Nb^{5+}.[5]

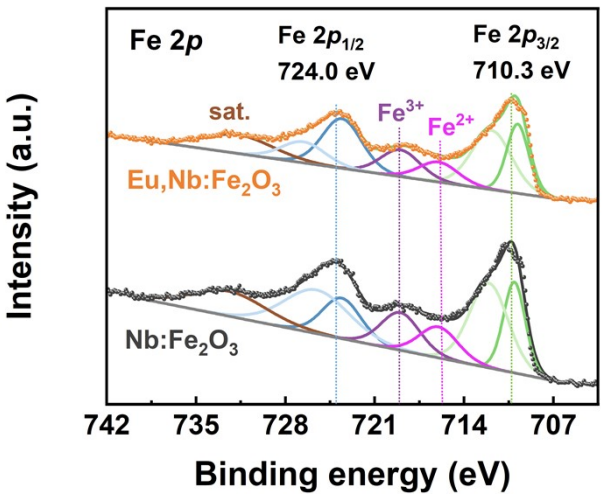

Figure S11. Comparison of surficial Fe 2*p* XPS spectra between Nb:Fe_2O_3 and Eu,Nb:Fe_2O_3 by HMA. The Fe 2*p* XPS spectra display Fe $2p_{1/2}$ (~724.0 eV) and Fe $2p_{3/2}$ (~710.3 eV) peaks,

accompanied by noticeable satellite peaks of Fe^{3+} (~719 eV) and Fe^{2+} (~716 eV), respectively.[6]

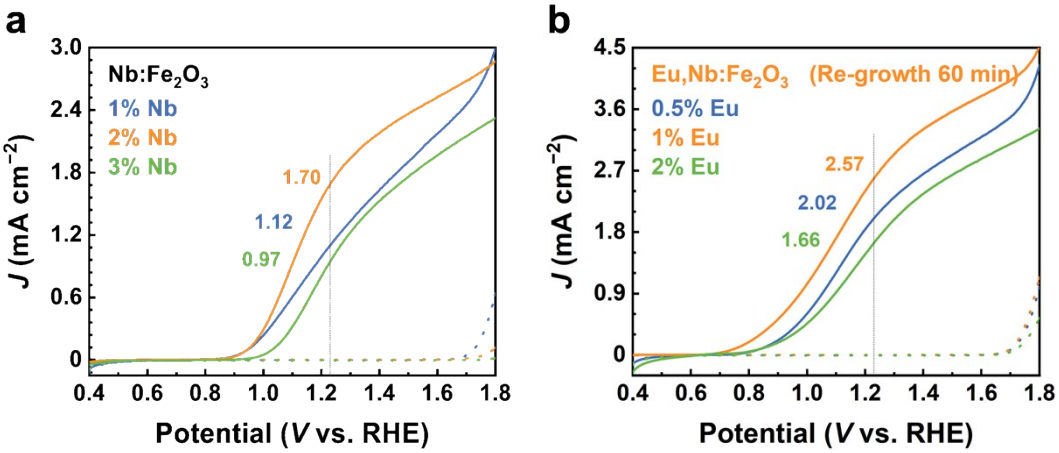

Figure S12. Optimizations of (a) $Nb:Fe_2O_3$ and (b) $Eu,Nb:Fe_2O_3$ photoanodes.

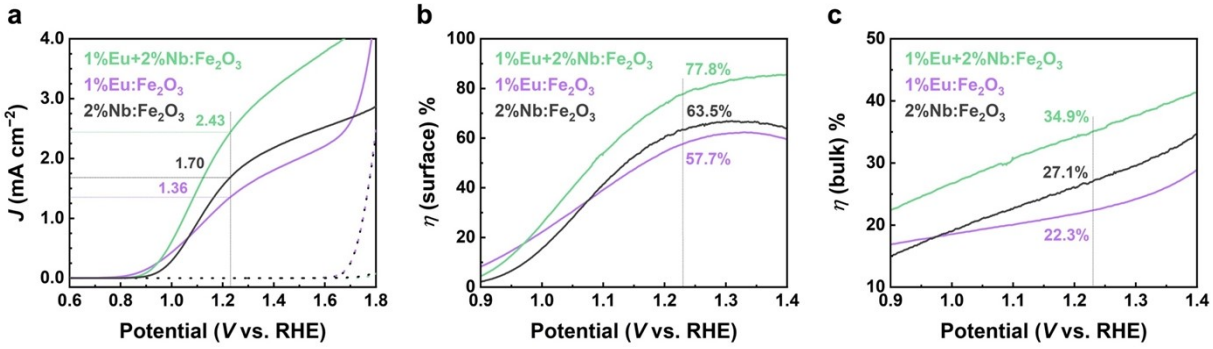

Figure S13. PEC performances of single Eu or Nb-doped and Eu, Nb co-doped Fe_2O_3 photoanodes with one-step hydrothermal method. The concentration of Nb and Eu in the precursor solution for hydrothermal growth is 2.0% (Nb/Fe) and 1.0% (Eu/Fe), respectively.

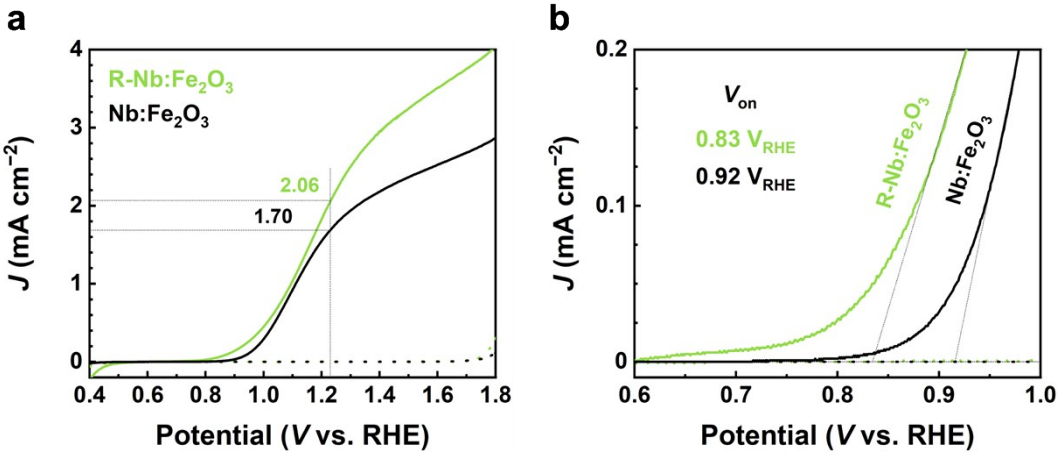

Figure S14. PEC performances of $Nb:Fe_2O_3$ and $R\text{-}Nb:Fe_2O_3$ photoanodes.

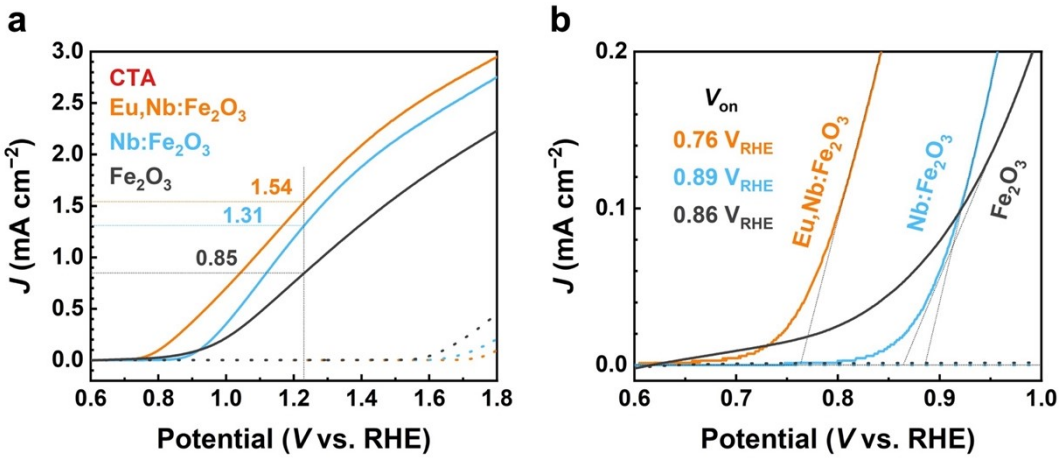

Figure S15. PEC performances of Fe_2O_3, Nb:Fe_2O_3 and Eu,Nb:Fe_2O_3 by CTA.

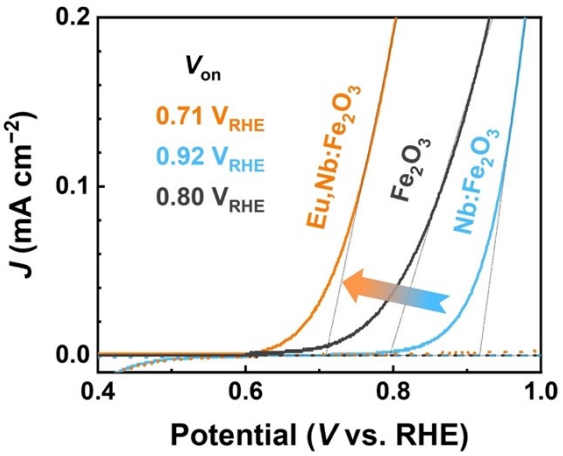

Figure S16. Extracted V_{on} of Fe_2O_3, Nb:Fe_2O_3 and Eu,Nb:Fe_2O_3 by HMA.

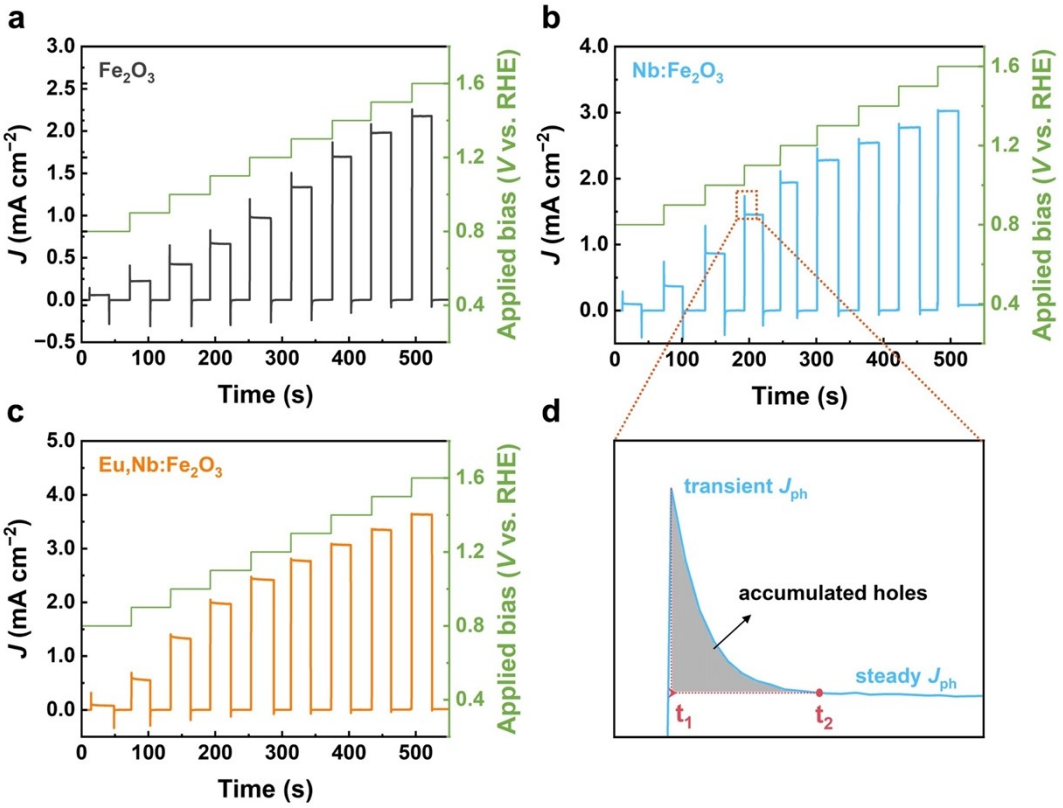

Figure S17. Chopped light chronoamperometry measurements of (a) Fe_2O_3, (b) Nb:Fe_2O_3 and (c) Eu,Nb:Fe_2O_3 by HMA between 0.8 and 1.6 V_{RHE} at an interval of 0.1 V_{RHE}. (d) The shadow area between t_1 and t_2 corresponds to the number of charges for the anodic transients. The number of holes accumulated at the surface of hematite photoanodes (Q_h) can be calculated by integrating the immediate photocurrent density I (I = transient J_{ph} – steady J_{ph}) as a function of time.

$$Q_h = \int_{t_1}^{t_2} I \, dt \qquad (6)$$

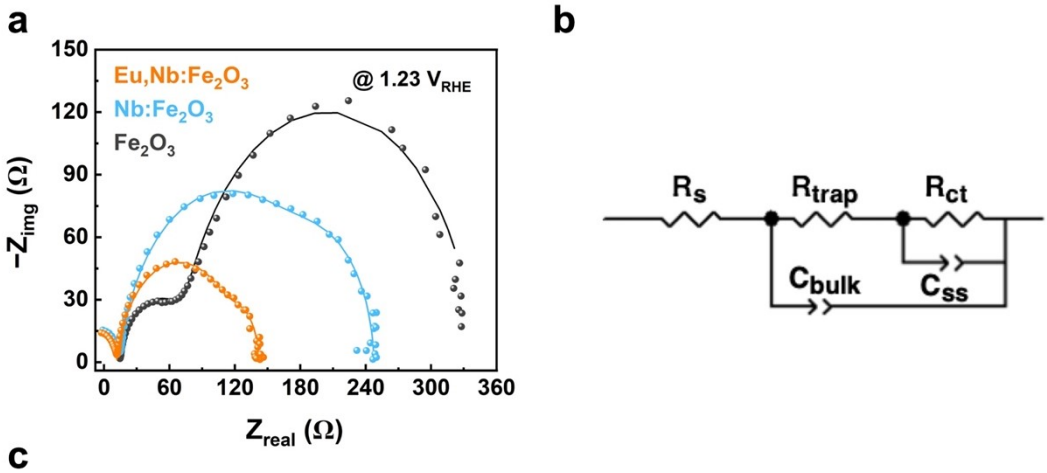

c

R (Ω) C (μF)	R_s	R_{trap}	R_{ct}	C_{bulk}	C_{ss}
Fe_2O_3	13.1	247.5	132.0	17.5	197
$Nb:Fe_2O_3$	14.2	193.4	40.1	32.6	279
$Eu,Nb:Fe_2O_3$	11.4	114.9	15.4	56.4	932

Figure S18. (a) Nyquist plots of Fe_2O_3, $Nb:Fe_2O_3$ and $Eu,Nb:Fe_2O_3$ by HMA. (b) A representative two-RC-unit equivalent circuit model used in this work. (c) Corresponding fitting results by Z-view software. R_s refers to the whole series resistance ascribed to the electrolyte, external contact and conductive substrate; R_{trap} refers to the charge trapping resistance in the semiconductor; R_{ct} refers to the charge transfer resistance of semiconductor/electrolyte interface; C_{bulk} refers to the capacitance in the depletion layer; C_{ss} refers to the capacitance of semiconductor/electrolyte interface.

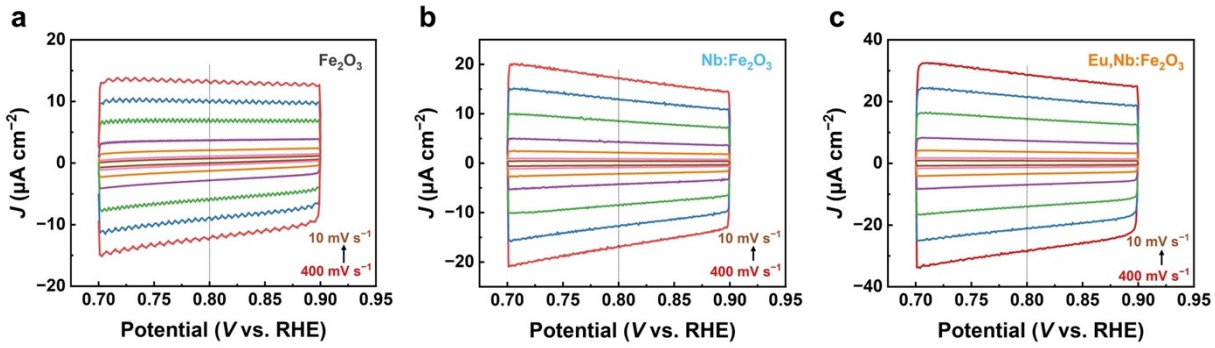

Figure S19. Cyclic voltammograms (CV) of (a) Fe_2O_3, (b) $Nb:Fe_2O_3$ and (c) $Eu,Nb:Fe_2O_3$ photoanodes obtained in the non-Faradaic region with a potential range of 0.7−0.9 V_{RHE} at scan rates of 10, 20, 50, 100, 200, 300 and 400 mV s^{-1}. The higher current obtained in the dark indicates that a larger electrical active area of the film allows more ions to be absorbed onto the electrical double layer. The ECSA was calculated using the equation: ECSA = C_{dl} / C_s, where C_s represents the specific capacitance of the active material under identical electrolyte conditions (C_s = 40 μF cm^{-2} in 1 M NaOH[7]).

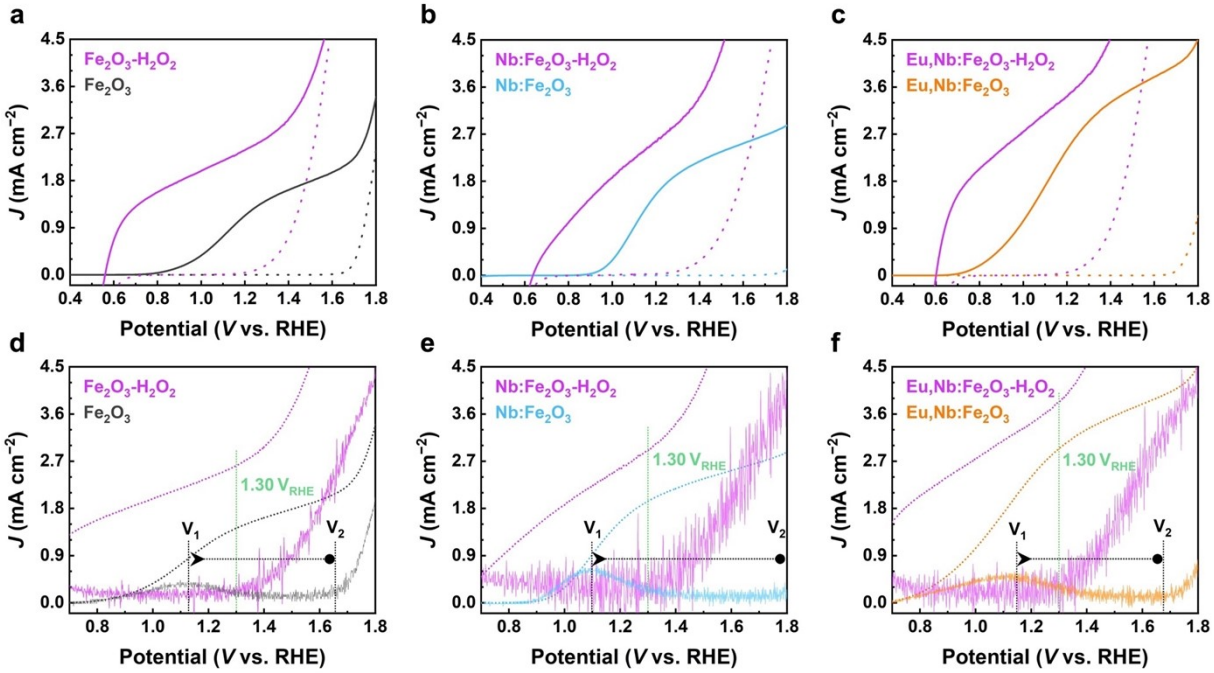

Figure S20. *J*–*V* curves of (a) Fe_2O_3, (b) Nb:Fe_2O_3 and (c) Eu,Nb:Fe_2O_3 measured in 1 M NaOH electrolyte with and without addition of 0.5 M H_2O_2. First-order differential of *J*–*V* curves (solid lines) for (c) Fe_2O_3, (d) Nb:Fe_2O_3 and (e) Eu,Nb:Fe_2O_3 measured in 1 M NaOH electrolyte with and without addition of 0.5 M H_2O_2, dash lines are their corresponding *J*–*V* curves. Bulk and surface carrier separation efficiencies are achieved in the same electrolyte with addition of 0.5 M H_2O_2, and can be calculated according to the following equations:

$$\eta_{bulk} = \frac{J_{H_2O_2}}{J_{abs}} \tag{7}$$

$$\eta_{surface} = \frac{J_{H_2O}}{J_{H_2O_2}} \tag{8}$$

where η_{bulk} denotes the fraction of holes reaching the electrode/electrolyte interface without recombining with electrons in the bulk, while $\eta_{surface}$ denotes the fraction of those holes at the interface that are injected to participate OER. J_{H_2O} and $J_{H_2O_2}$ are photocurrent densities of water oxidation in 1 M NaOH without and with addition of H_2O_2, respectively. J_{abs} is the expected photocurrent when absorbed photons are completely converted into current. Note that $\eta_{surface}$ of H_2O_2 oxidation is 1 in the case of no hole injection barrier existing.

J_{abs} can be calculated according to the correlation between absorbance and irradiation:

$$P_{abs} = P_0 (1 - 10^{-A}) \tag{9}$$

P_0 (mW cm^{-2} nm^{-1}) is power provided by solar simulator (AM 1.5 G), P_{abs} is power of light actually absorbed by photoanode. *A* is absorbance of photoanode and light harvesting efficiency

(LHE) is defined as $1 - 10^{-A}$. Integration of P_{abs} (λ) (mW cm^{-2} nm^{-1}) along with wavelength λ gives the total power density (unit of mW cm^{-2}), which is the maximum power of photoanode. Absorption photocurrents (J_{abs}) of Fe_2O_3 (10.41 mA cm^{-2}, <577 nm), Nb:Fe_2O_3 (9.83 mA cm^{-2}, <577 nm) and Eu,Nb:Fe_2O_3 (10.42 mA cm^{-2}, <579 nm). The following formula shows the power of light absorbed by photoanode (J_{abs}):

$$J_{abs} = \int_{\lambda_1}^{\lambda_2} \frac{\lambda}{1240} P_{abs}\, d\lambda \tag{10}$$

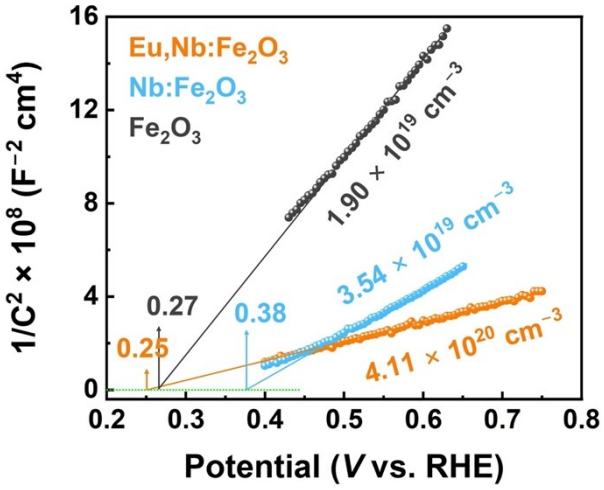

Figure S21. Mott−Schottky (M−S) plots of Fe_2O_3, Nb:Fe_2O_3 and Eu,Nb:Fe_2O_3 by HMA. The required kinetic overpotential for OER is equivalent to the difference between V_{on} and E_{FB}.[8] Eu,Nb:Fe_2O_3 gives a smaller difference of ~440 mV between V_{on} and E_{FB} than that of Nb:Fe_2O_3 (540 mV) and Fe_2O_3 (530 mV), providing the evidence of the reduced overpotential.

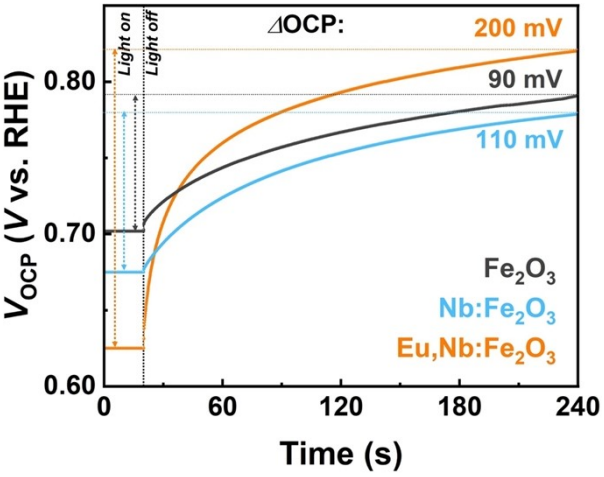

Figure S22. OCP transient decay profiles of Fe_2O_3, Nb:Fe_2O_3 and Eu,Nb:Fe_2O_3.

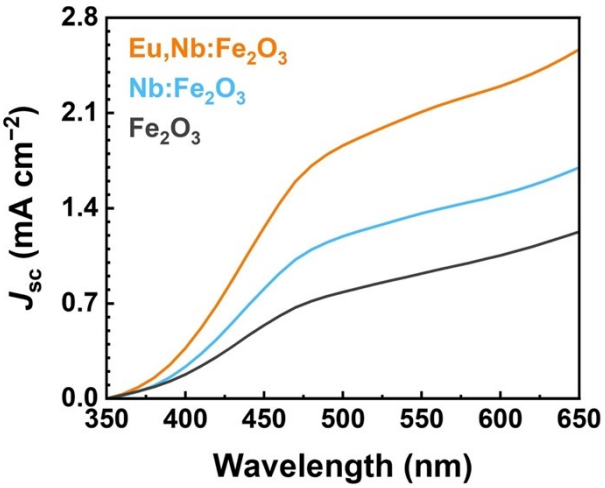

Figure S23. Solar photocurrent density (J_{sc}) by IPCE. The integrated IPCE with respect to the AM 1.5 G spectrum at 1.23 V_{RHE} provides J_{sc} of 1.22, 1.68 and 2.54 mA cm^{-2} for Fe_2O_3, Nb:Fe_2O_3 and Eu,Nb:Fe_2O_3, respectively.

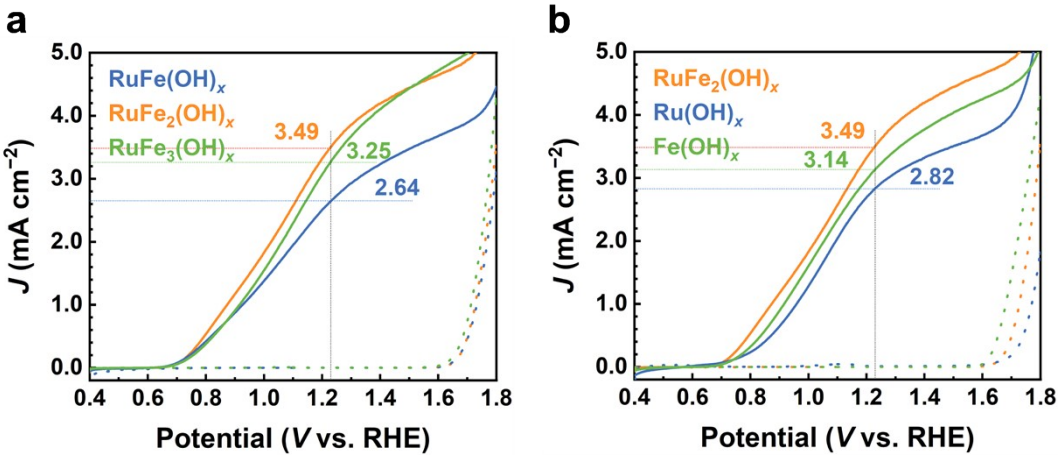

Figure S24. Optimization of co-catalyst loading on Eu,Nb:Fe_2O_3 photoanode.

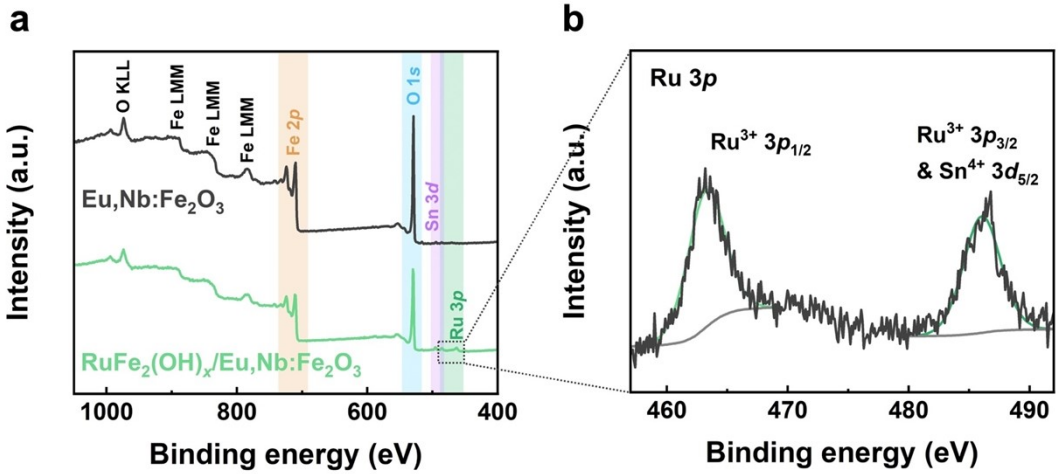

Figure S25. (a) XPS survey spectra of Eu,Nb:Fe_2O_3 before and after loading $RuFe_2(OH)_x$. (b) Ru 3*p* XPS spectrum. We determined the composition of $RuFe_2(OH)_x$ by calculating the increased surface Ru, Fe and O contents after loading $RuFe_2(OH)_x$, where the ratio of Ru:Fe:O is approximately 1:2:6.75. The source material used to prepare $RuFe_2(OH)_x$ is $FeCl_3$ (Fe^{3+}) and $RuCl_3$ (Ru^{3+}), and in Ru 3*p* XPS spectrum (b), the peaks at 463.3 eV and 486.1 eV can be ascribed to Ru^{3+} $3p_{3/2}$ and Ru^{3+} $3p_{1/2}$, respectively.[9] Finally, the x value is concluded to be about 7.

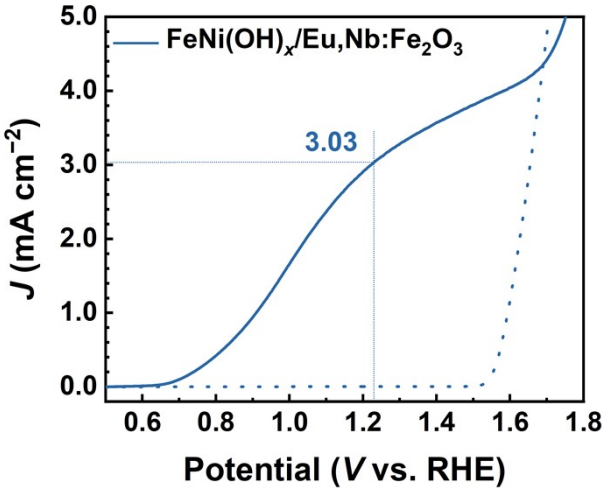

Figure S26. *J*–*V* curves of the optimized $FeNi(OH)_x$/Eu,Nb:Fe_2O_3 photoanode. For co-catalyst $FeNi(OH)_x$ modification, the prepared photoanode was immersed into a mixed aqueous solution containing 5 mM $NiCl_2 \cdot 6H_2O$ (Aladdin, 99.0%) and 5 mM $FeCl_3 \cdot 6H_2O$ (Aladdin, 99.0%) for 10 min at room temperature. Subsequently, the photoanode was dipped into 1 M NaOH immediately for several seconds to form oxyhydroxides.

Table S1. Performances of recently reported hematite photoanodes with different dopants.

Dopant type	Porous hematite /with co-catalyst	J_{ph} at ~1.23 V_{RHE} (mA cm^{-2})	V_{on} (V_{RHE})	Electrolyte	Reference
Ti, Si	Ti-(SiO_x/np-Fe_2O_3) /with Co-Pi *	2.44 3.19	0.95 0.80	1M NaOH	[10]*Angew. Chem. Int. Ed.*, 2016, **55**, 9922–9926
Ti	TiO_2/Fe_2O_3 /with Co-Pi *	0.61 0.91	~0.90 0.76	1M NaOH	[11]*Chem. Eng. J.*, 2017, **320**, 81–92
Zr	Zr-Fe_2O_3 /with Co-Pi *	1.50 1.87	0.85 0.65	1M KOH	[12]*Angew. Chem. Int. Ed.*, 2017, **56**, 4150–4155
Ti	Ti-Fe_2O_3 /with CoP *	1.53 2.1	0.87 0.77	1M NaOH	[13]*J. Catal.*, 2018, **366**, 275–281
–	RD-Fe_2O_3 *	2.0	0.95	1M KOH	[14]*ACS Appl. Mater. Interfaces*, 2018, **10**, 10141–10146
Ti	Ti:Fe_2O_3 /with Co-Pi	1.20 2.70	0.74 0.64	1M KOH	[15]*Adv. Funct. Mater.*, 2019, **29**, 1801902
Nb, Sn	Nb,Sn:Fe_2O_3@$FeNbO_4$ /with $NiFeO_x$	2.24 2.71	0.80 0.71	1M NaOH	[16]*ACS Catal.*, 2019, **9**, 1289–1297
Zr	Zr:Fe_2O_3@ZrO_2	1.55	0.77	1M NaOH	[17]*Chem. Eng. J.*, 2020, **390**, 124504
–	Fe_2O_3/Fe_3O_4 NT *	~0.35	0.56	1M NaOH	[18]*J. Alloys Compd.*, 2022, **918**, 165787
Ce	Ce:Fe_2O_3@Fe_2O_3 /with photoactivation	1.48 1.92	0.67 0.64	1M NaOH	[19]*Chem. Eng. J.*, 2022, **448**, 137602
P, Ti	P,Ti:Fe_2O_3 /with $NiFeO_x$ *	2.50 3.54	0.90 0.79	1M NaOH	[6]*Nano Energy*, 2023, **107**, 108090
Eu, Nb	**Eu,Nb:Fe_2O_3 /with $RuFe_2(OH)_x$ ***	**2.57 3.49**	**0.71 0.67**	1M NaOH	**this work**

NS: nanosheet; RD: rapid dehydration; NR: nanorod; NC: nanocube; PH: porous hematite; NT: nanotube; P_{Si}: siloxane-modified π-conjugated polymer.

* porous structure

References

1 A. Zaban, M. Greenshtein and J. Bisquert, *ChemPhysChem*, 2003, **4**, 859–864.

2 W. Shockley, *Bell Syst. tech. j*, 1949, **28**, 435–489.

3 Z. J. Zhang, H. Nagashima and T. Tachikawa, *Angew. Chem. Int. Ed.*, 2020, **59**, 9047–9054.

4 P. Peerakiatkhajohn, J. H. Yun, H. J. Chen, M. Q. Lyu, T. Butburee and L. Z. Wang, *Adv. Mater.*, 2016, **28**, 6405–6410.

5 Z. Y. Chen, Y. T. Ye, X. Y. Feng, Y. Wang, X. W. Han, Y. Zhu, S. Wu, S. Wang, W. Yang, L. Wang and J. Zhang, *Nat. Commun.*, 2023, **14**, 2000.

6 J. H. Kang, K. Y. Yoon, J. E. Lee, J. Park, S. Chaule and J. H. Jang, *Nano Energy*, 2023, **107**, 108090.

7 C. C. L. McCrory, S. Jung, J. C. Peters and T. F. Jaramillo, *J. Am. Chem. Soc.*, 2013, **135**, 16977–16987.

8 Z. Chen, H. Dinh and E. Miller, *Photoelectrochemical water splitting: standards, experimental methods, and protocols*, Springer, 2013.

9 Q. Lu, Y. Guo, P. Mao, K. M. Liao, X. H. Zou, J. Dai, P. Tan, R. Ran, W. Zhou, M. Ni and Z. P. Shao, *Energy Storage Mater.*, 2020, **32**, 20–29.

10 H. J. Ahn, K. Y. Yoon, M. J. Kwak and J. H. Jang, *Angew. Chem. Int. Ed.*, 2016, **55**, 9922–9926.

11 P. S. Shinde, M. A. Mahadik, S. Y. Lee, J. Ryu, S. H. Choi and J. S. Jang, *Chem. Eng. J.*, 2017, **320**, 81–92.

12 C. C. Li, A. Li, Z. B. Luo, J. J. Zhang, X. X. Chang, Z. Q. Huang, T. Wang and J. L. Gong, *Angew. Chem. Int. Ed.*, 2017, **56**, 4150–4155.

13 D. C. Jiang, Q. D. Yue, S. Tang, L. Zhang, L. Zhu and P. W. Du, *J. Catal.*, 2018, **366**, 275–281.

14 A. Z. Liao, H. C. He, L. Q. Tang, Y. C. Li, J. Y. Zhang, J. N. Chen, L. Chen, C. F. Zhang, Y. Zhou and Z. G. Zou, *ACS Appl. Mater. Interfaces*, 2018, **10**, 10141–10146.

15 S. S. Yi, B. R. Wulan, J. M. Yan and Q. Jiang, *Adv. Funct. Mater.*, 2019, **29**, 1801902.

16 H. M. Zhang, Y. K. Kim, H. Y. Jeong and J. S. Lee, *ACS Catal.*, 2019, **9**, 1289–1297.

17 I. Kwon Jeong, M. A. Mahadik, S. Kim, H. M. Pathan, W.-S. Chae, H. Suk Chung, G. Won Kong, S. Hee Choi and J. Suk Jang, *Chem. Eng. J.*, 2020, **390**, 124504.

18 J. B. Xue, N. R. Zhang, Q. Q. Shen, Q. Li, X. G. Liu, H. S. Jia and R. F. Guan, *J. Alloys Compd.*, 2022, **918**, 165787.

19 J. W. Bai, R. T. Gao, X. T. Guo, J. L. He, X. H. Liu, X. Y. Zhang and L. Wang, *Chem. Eng. J.*, 2022, **448**, 137602.